Journal of
Composites Science

Article

Porous $NiMoO_4$-NrGO as a Battery-Like Electrode Material for Aqueous Hybrid Supercapacitors

Shahrzad Arshadi-Rastabi [1,2,*], Rasoul Sarraf-Mamoory [1,*], Ghadir Razaz [2], Nicklas Blomquist [2], Jonas Örtegren [2] and Håkan Olin [2]

[1] Department of Materials Engineering, Tarbiat Modares University, Tehran 14115111, Iran
[2] Department of Natural Sciences, Mid Sweden University, 85170 Sundsvall, Sweden; ghadir.razaz@miun.se (G.R.); nicklas.blomquist@miun.se (N.B.); jonas.ortegren@miun.se (J.Ö.); hakan.olin@miun.se (H.O.)
* Correspondence: shahrzad.arshadi@modares.ac.ir (S.A.-R.); rsarrafm@modares.ac.ir (R.S.-M.); Tel.: +98-82883308 (R.S.-M.)

Abstract: Recently, much research has investigated nanocomposites and their properties for the development of energy storage systems. Supercapacitor performance is usually enhanced by the use of porous electrode structures, which produce a larger surface area for reaction. In this work, a biocompatible polymer of starch medium was used to create the porous nanostructure. Two powders, i.e., Nickel molybdate/reduced graphene oxide ($NiMoO_4$-rGO) and Nickel molybdate/nitrogen-doped reduced graphene oxide ($NiMoO_4$-NrGO), were synthesized using the deposition method in a medium containing starch, nickel nitrate salts, sodium molybdate, and graphene oxide powder. In terms of electrochemical performance, the $NiMoO_4$-NrGO electrode displayed a higher specific capacitance, i.e., 932 Fg^{-1} (466 Cg^{-1}), than the $NiMoO_4$-rGO electrode, i.e., 884 Fg^{-1} (442 Cg^{-1}), at a current density of 1 Ag^{-1}. In fact, graphene oxide sheets could lose more oxygen groups in the presence of ammonia, resulting in increased electrical conductivity. For the asymmetric supercapacitor of $NiMoO_4$-NrGO//AC, the specific capacitance at 1 Ag^{-1}, energy density, and power density were 101.2 Fg^{-1} (111.32 Cg^{-1}), 17 Wh kg^{-1}, and 174.4 kW kg^{-1}, respectively. In addition, this supercapacitor material displayed a good cycling stability of over 82%.

Keywords: porous nanostructure; deposition method; $NiMoO_4$-rGO; biocompatible polymer; electrochemical performance; asymmetric supercapacitor of $NiMoO_4$-NrGO//AC

Citation: Arshadi-Rastabi, S.; Sarraf-Mamoory, R.; Razaz, G.; Blomquist, N.; Örtegren, J.; Olin, H. Porous $NiMoO_4$-NrGO as a Battery-Like Electrode Material for Aqueous Hybrid Supercapacitors. *J. Compos. Sci.* **2023**, *7*, 217. https://doi.org/10.3390/jcs7060217

Academic Editor: Vincenza Brancato

Received: 31 March 2023
Revised: 13 May 2023
Accepted: 22 May 2023
Published: 26 May 2023

1. Introduction

Energy is among the most important issues facing the world today. Decreasing fossil fuel sources and their environmental problems has compelled scientists to strive to replace them with renewable and clean energy sources [1,2]. Various energy storage systems such as batteries and supercapacitors have recently been developed, and supercapacitors have attracted particular interest. The limitations of batteries have restricted their use in systems that require high power density [3,4]. Compared with batteries, supercapacitors have about 10 times the power density and a faster charge–discharge cycle of 1~30 s. Different category of materials such as carbonic, polymeric, and metal oxide/hydroxide materials have been used in supercapacitors, with metal oxides commonly being utilized due to their unique properties [5]. In addition to single metal oxides such as MnO_2 [6], Co_3O_4 [7], NiO [8], and RuO_2 [9], binary metal oxides such as $CoMoO_4$ [10], $NiMoO_4$ [11], and $MnMoO_4$ [12] are considered promising electrode materials. Compared with single metal oxides, binary metal oxides with multiple oxidation states and high electrical conductivity enhance energy storage systems. Meanwhile, metal molybdates are an important group of inorganic materials that provide high electrical conductivity. However, the high electrical conductivity, low price, abundance, and good chemical and thermal stability of $NiMoO_4$ make it an appropriate alternative to use as an electrode in supercapacitors [13]. $NiMoO_4$ is synthesized using different techniques and apparatuses in, for example, hydrothermal [14,15], microwave [16], sonochemical [17], and sol–gel [18] synthesis. Various forms of $NiMoO_4$, such as nanorod [11], nanocluster [19], nanosphere [20], flower-like [21], and nanoplate [22] $NiMoO_4$, have been synthesized and explored.

Based on literatures, using the "pseudocapacitive" or the "battery-type" for Ni-based material such as $NiMoO_4$ is still controversial [23]. Nickel molybdate ($NiMoO_4$) displays oxidation–reduction (redox) behavior and also has a good specific capacitance. $NiMoO_4$ is a combination of MoO_3 and NiO metal oxides. The strong redox reaction of Ni^{2+} ions and the good electrical conductivity of $MoO_4{}^{2-}$ ions make $NiMoO_4$ highly suitable for use as an electrode material in supercapacitors [13,24]. $NiMoO_4$ has better supercapacitor properties than its binary compounds MoO_3, with a specific capacitance of 176 Fg^{-1} [25], and NiO, with a specific capacitance of 414.6 Fg^{-1} [26]. In addition, utilizing carbon materials such as activated carbon (AC), carbon nanotubes (CNT), and three-dimensional (3D) graphene as a scaffold for the metal oxide $NiMoO_4$ results in enhanced electrical conductivity, chemical stability, and ultimately enhancement of supercapacitor performance [27]. The 3D network structure of graphene provides many electron transfer paths and active sites, and also favors mechanical stability during cycling performance.

This research aimed to create a 3D structure of reduced graphene oxide and nickel molybdate to combine the beneficial properties of both materials and eventually enhance the performance of supercapacitors. The $NiMoO_4$-NrGO and AC electrodes were applied to construct an asymmetric supercapacitor. The electrochemical performance of the fabricated supercapacitor was investigated by cyclic voltammetry (CV), galvanostatic charge–discharge (GCD), electrical resistivity (EIS), and cycling performance tests using a potentiostat. The material for the synthesized electrode was characterized using different techniques. In addition, to optimize the electrolyte, the effect of pH on the electrochemical behavior of the NMO-NrGO electrode and the optimal electrolyte concentration to use in the whole supercapacitor cell were investigated.

2. Experimental Section

2.1. Materials and Methods

The primary chemical materials used in this research along with their specifications are given in Table S1.

2.2. Preparation of $NiMoO_4$-rGO and $NiMoO_4$/N-Doped rGO Hybrid Nanocomposite

The following steps were used to synthesize the powders of $NiMoO_4$-rGO and $NiMoO_4$/N-doped rGO hybrid nanocomposite through a precipitation method: (a) a solution containing 1 g starch in 20 mL distilled water was prepared at 80 °C to provide a gelation suspension; (b) 1 mg graphene oxide was dispersed in 20 mL distilled water and added to the starch suspension; (c) 3.0 mL ammonia (28 wt%) was added to the suspension of starch and graphene oxide to adjust the pH to about 10; (d) two solutions containing 20 mL of 5 mM $Ni(NO_3)_2 \cdot 6H_2O$ and 20 mL of 5 mM $Na_2MoO_4 \cdot 2H_2O$, respectively, were added drop-wise to the suspension of starch, graphene oxide, and ammonia under continuous stirring for 1 h at a temperature of 80 °C; (e) the synthesized powders were washed with distilled water to remove the extra materials and impurities. The powders dried in a vacuum oven at a temperature of 60 °C for 24 h; (f) the final powders were calcinated in a tube furnace with Ar atmosphere at a temperature of 350 °C for 2 h; and (g) finally, two groups of powder were synthesized and labeled: $NiMoO_4$/reduced graphene oxide (NMO-rGO) and $NiMoO_4$/N-doped reduced graphene oxide (NMO-NrGO). Note that step (c) was not performed when synthesizing NMO-rGO. The process of synthesizing the electrode materials is schematically illustrated in Figure 1.

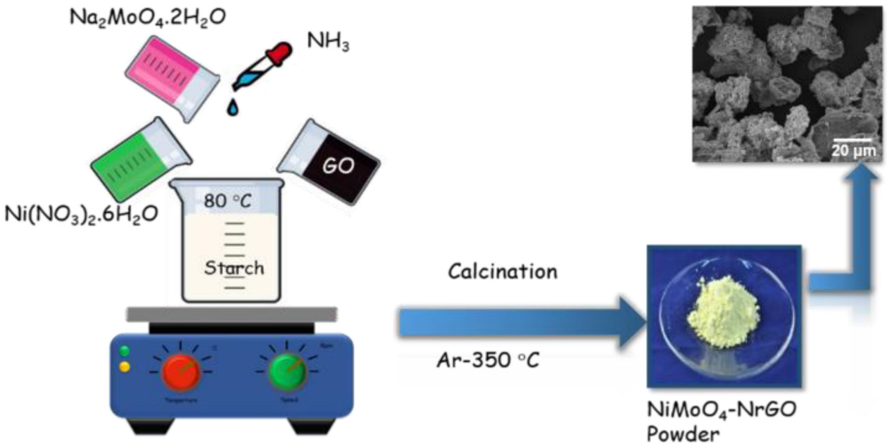

Figure 1. Schematic image of synthesizing the electrode materials.

2.3. Preparation of $NiMoO_4$-rGO and $NiMoO_4$-NrGO Hybrid Electrodes Using Ni Foam Current Collectors

First, the nickel foam was immersed in the ultrasonic bath of 1 M HCl (37 wt%) for 5 min to remove the impurities from the surface; then, it was cleaned with water and ethanol. The synthesized powders (80 wt%), AC (10 wt% AC), and polyvinylidene fluoride binder (10 wt% PVDF) were mixed in an ultrasonic bath. The nickel foam was then uniformly coated with this mixture. Next, the electrodes were dried at the temperature of 60 °C for 24 h in an oven. All electrodes were soaked in the 3.0 M KOH electrolyte for 30 min before the electrochemical tests, all of which were performed at room temperature.

2.4. Material Characterization

To characterize and study the properties of NMO-rGO and NMO-NrGO samples, various analytical methods such as X-ray diffraction (XRD Bruker 2D phaser with Cu K_α radiation ($\lambda = 0.1542$ nm, Bremen, Germany), scanning electron microscopy (TESCAN MIRA3 SEM, Brno, Czech Republic), and Fourier-transform infrared spectroscopy (ABB Bomem FTIR system, ATR method, Västerås, Sweden) were used. Furthermore, Brunauer–Emmett–Teller (BET) and Barrett–Joyner–Halenda (BJH) gas adsorption measurements (Micromeritics TriStar II analyzer, Norcross, GA, USA) were used to study the specific surface area and pore size distribution of the materials.

2.5. Electrochemical Investigations

The electrochemical performance of NMO-rGO and NMO-NrGO electrodes was measured using a potentiostat instrument (VersaStat 2.63.3) with different modes, such as CV, GCD, and electrochemical impedance spectroscopy (EIS). The synthesized electrodes were investigated as working electrodes in a three-electrode setup. The reference and counter electrodes were calomel and platinum, respectively, and the electrolyte was 3.0 M KOH. CV was performed in the voltage range of 0–0.7 V at scan rates of 5–100 mV s^{-1}. GCD tests were conducted in the voltage range of 0–0.5 V at current densities of 1–50 Ag^{-1}. Electrochemical impedance spectroscopy (EIS) measurements were carried out at 0.1–100 KHz and a voltage amplitude of 10 mV. To build an asymmetric supercapacitor, AC electrode, NMO-NrGO electrode, and cellulose paper were used as the negative electrode, positive electrode, and separator, respectively. The specific capacitance is calculated based on the equations in supplementary [28,29].

3. Results and Discussion

3.1. Material Characterization of the Electrodes

Figure 2a shows the FTIR spectra of the pure GO, NMO-rGO, and NMO-NrGO nanocomposites in the range from 400–4000 cm^{-1}. Based on the FTIR spectrum of GO, most of the peaks are attributed to the graphene oxide functional groups. These correspond to the C=O carbonyl group (~1765 cm^{-1}), aromatic C=C bonds (~1650 cm^{-1}), the C–OH bond (~1397 cm^{-1}), deformation of the C–O–C bond (~1208 cm^{-1}), and C–O bonds (~1038 cm^{-1}) [30,31]. Furthermore, a broad band of the hydroxyl (O–H) group between ~2800 and ~3600 cm^{-1} contributed to the water molecules adsorbed on the surface of the samples [32]. The FTIR spectra of the NMO-rGO and NMO-NrGO nanocomposites show that the strong absorption peak at 3250 cm^{-1} is reduced significantly, which confirms the transformation of GO to rGO [33] after compositing with $NiMoO_4$. In addition, as can be seen in the FTIR spectra of the NMO-rGO and NMO-NrGO nanocomposites, the oxygenated groups of C–OH, C–O, C=O, and C–O–C either disappeared or weakened. This also supports the reduction of GO sheets to rGO during the adsorption of Ni^{2+} to the negatively charged oxygenated groups of graphene oxide [34]. The characteristic bonds at 444, 750, and 836 cm^{-1}, respectively, are related to Mo–O–Mo, the Mo–O–Ni vibration mode, and the Mo=O bond of $NiMoO_4$ [35,36].

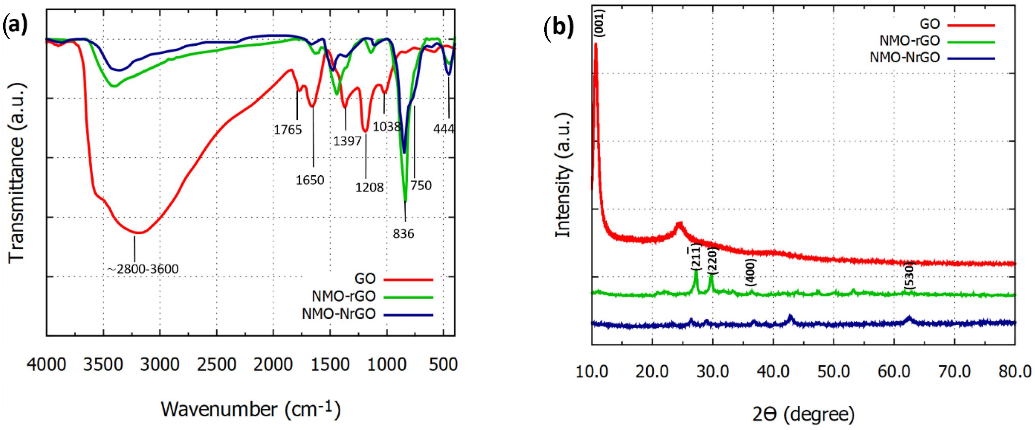

Figure 2. (**a**) Fourier–transform infrared spectrometry (FTIR) spectra; (**b**) X-ray diffraction (XRD) patterns of the pure GO, NMO-rGO, and NMO-NrGO nanocomposites.

Figure 2b illustrates the XRD patterns of the GO, NMO-rGO, and NMO-NrGO nanocomposites. It can be observed that a sharp peak for GO appearing at $2\theta = 10.6°$ (002) is absent for the NMO-rGO and NMO-NrGO nanocomposites. This implies the reduction in oxygen groups after compositing with $NiMoO_4$ and heating at 350 °C [37,38]. Other peaks occurring in NMO-rGO and NMO-NrGO nanocomposite patterns with high intensity are attributed to the crystalline $NiMoO_4$ nanoparticles [38,39]. Based on the standard diffraction pattern data other papers [36,40,41], the JCPDS code number of the $NiMoO_4$ powder is 00-045-0142.

The SEM images of the NMO-rGO and NMO-NrGO nanocomposites are presented in Figure 3a–d. These show the $NiMoO_4$ nanorods decorating the rGO sheets, providing a 3D structure and forming many porosities through the nanorods. This porous nanostructure provides short diffusion paths that enhance the accessibility of the reaction sites to the electrolyte. This increases the charge transfer and thus the energy and power density [34]. The electrostatic attachment of metal ions to the functional groups of the GO sheets results in the reduction of GO to rGO and then the growth of $NiMoO_4$ nanoparticles on the rGO sheets [31,36,42]. Based on the SEM images of the NMO-NrGO nanocomposite (Figure 3c,d), relatively thick rGO sheets can be seen, which could be a sign of multilayered graphite. This phenomenon can be due to the effect of ammonia on reducing the graphene oxide functional groups [38]. It can be concluded that the formation of hydrogen bonds between the functional groups and free electrons of ammonia resulted in more reduction in graphene oxide. This neutralized the surface charge of the graphene oxide sheets as well as reducing the electrostatic repulsion between the graphene oxide sheets and increasing their adhesion, thereby producing multilayered graphite.

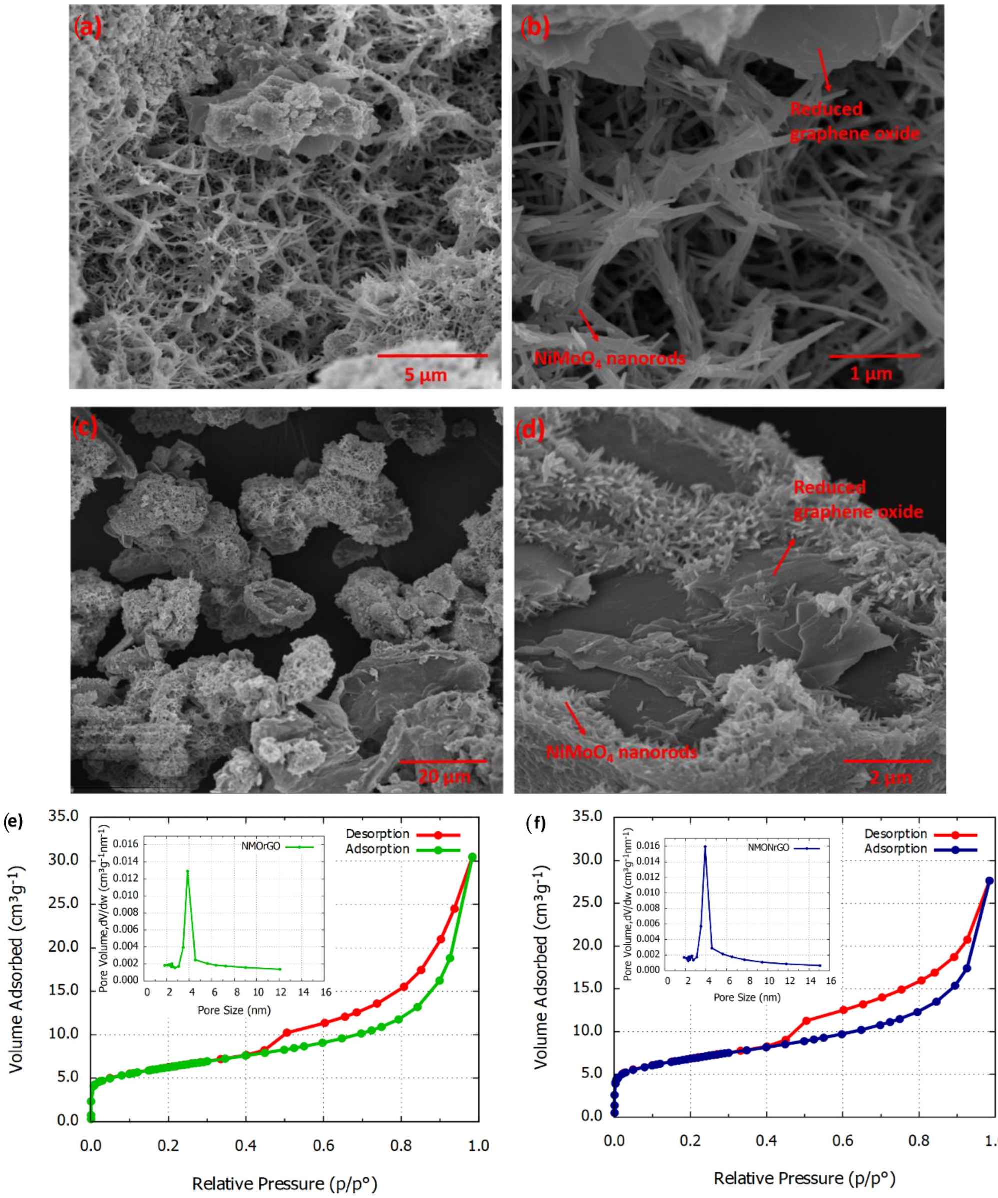

Figure 3. SEM images of: NMO-rGO nanocomposite at (**a**) low magnification and (**b**) high magnification; and NMO-NrGO nanocomposite at (**c**) low magnification and (**d**) high magnification. BET adsorption–desorption isotherm with BJH plot of pore size distribution (inset) for (**e**) NMO-rGO and (**f**) NMO-NrGO nanocomposites.

Furthermore, the N_2 adsorption–desorption isotherms using BET and the size distribution of the pores using BJH are given in Figure 3e,f. For the porous nanostructure of NMO-rGO, the specific surface area and the average volume of pores are calculated as 23.8 $m^2\ g^{-1}$ and 0.41 $cm^3\ g^{-1}$, respectively, whereas the specific surface area and the average volume of pores for the NMO-NrGO nanocomposite are 22.3 $m^2\ g^{-1}$ and 0.38 $cm^3\ g^{-1}$, respectively.

3.2. Electrochemical Properties of NMO-rGO and NMO-NrGO Electrodes

Figure 4a shows the CV curves of NMO-rGO and NMO-NrGO electrodes at a scan rate of 10 mV s^{-1}. Comparison of the obtained specific capacitances and the areas under the curves indicates a higher specific capacitance for the NMO-NrGO than the NMO-rGO electrode. As can be seen in Figure 3e,f, the specific areas for both the NMO-rGO and NMO-NrGO electrodes are similar. Thus, the enhancement of the specific capacitance of the NMO-NrGO electrode versus the NMO-rGO electrode could not be due to surface area reaction. It can be said that the removal of a large percentage of the oxygenated functional groups attached to the GO sheets in the alkaline environment of ammonia led to an increase in the electrical conductivity of the rGO sheets and an increase in the energy storage capacitance [43]. In addition, the potential difference (ΔE) between the anodic and cathodic peaks in the NMO-NrGO electrode is less than in the NMO-rGO electrode. This indicates that the greater reduction in GO also enhanced the electrochemical reversibility of the NMO-NrGO electrode [44]. Figure 4b shows the GCD curves of the NMO-rGO and NMO-NrGO electrodes in the voltage range of 0–0.5 V at a current density of 1 Ag^{-1}. The NMO-rGO and NMO-NrGO electrodes display specific capacitances of 884 Fg^{-1} (442 Cg^{-1}) and 932 Fg^{-1} (466 Cg^{-1}), respectively. The nonlinear shape of the GCD curves and the presence of a pair of voltage plateaus at voltages of about 0.2 and 0.3 V show that the specific capacitances of both electrodes were affected by the Faradaic reactions of Ni^{2+}/Ni^{3+} ions in the $NiMoO_4$ nanoparticles [45,46], agreeing with the CV results. Figure 4c shows the specific capacitances of the NMO-rGO and NMO-NrGO electrodes versus different scan rates of 10–100 mV s^{-1}. The curves show that increasing the scan rate decreases the specific capacitance for both electrodes. The highest specific capacitance value was obtained at a scan rate of 10 Ag^{-1}, equivalent to 411.42 Fg^{-1} (288 Cg^{-1}) and 495.7 Fg^{-1} (347 Cg^{-1}) for NMO-rGO and NMO-NrGO electrodes, respectively. The bar chart in Figure 4d illustrates the specific capacitance–current density diagram for the NMO-rGO and NMO-NrGO electrodes. It is observed that the specific capacitances of both electrodes decreased with the increase in current density from 1 to 100 Ag^{-1}. The decrease in the specific capacitance can be attributed to the voltage drop, insufficient active sites, and high-speed redox reactions [47]. At high current densities, ions cannot transfer as quickly as electrons, so the ions limit the redox process and the electron transfer. Thus, a limited number of electrolyte ions penetrate the electroactive materials. Furthermore, because it is mostly the outer layers of the electroactive materials that are involved in the charge storage process, small amounts of the active materials are involved in the redox reactions [48,49]. The highest specific capacitance value for the NMO-NrGO electrode was obtained at a current density of 1 Ag^{-1}, which is equivalent to 932 Fg^{-1} (466 Cg^{-1}). As can be seen, at the current density of 50 Ag^{-1}, the capacitance retention of NMO-NrGO electrode was about 52%, whereas the capacitance retention of the NMO-rGO electrode calculated around 8%. It demonstrates the better performance of the NMO-NrGO nanocomposite to use in supercapacitors at high current densities. Figure 4e shows the cycling performance of the NMO-rGO and NMO-NrGO electrodes at a current density of 2 Ag^{-1} and in the voltage range of 0–0.5 V. Both electrodes started with a high specific capacitance of approximately 800 Ag^{-1} (400 Cg^{-1}). The cycling performance of the NMO-rGO electrode initially decreased rapidly, but the degradation rate slowed after 50 cycles. The NMO-NrGO electrode displayed more specific capacitance and stable cycling performance over 500 cycles, finally retaining 76% of its specific capacitance in the first cycle. In addition, multiple types of electrolytes, including acidic (H_2SO_4), alkaline (KOH), and neutral (Na_2SO_4) electrolytes, were employed to evaluate the impact of pH and electrolyte concentration on the electrochemical behavior of the NMO-NrGO electrode. KOH electrolyte was used at a variety of concentrations, including 1.0, 2.0, 3.0, and 4.0 M [50–52]. The resultant CV curves are shown in Figure S2.

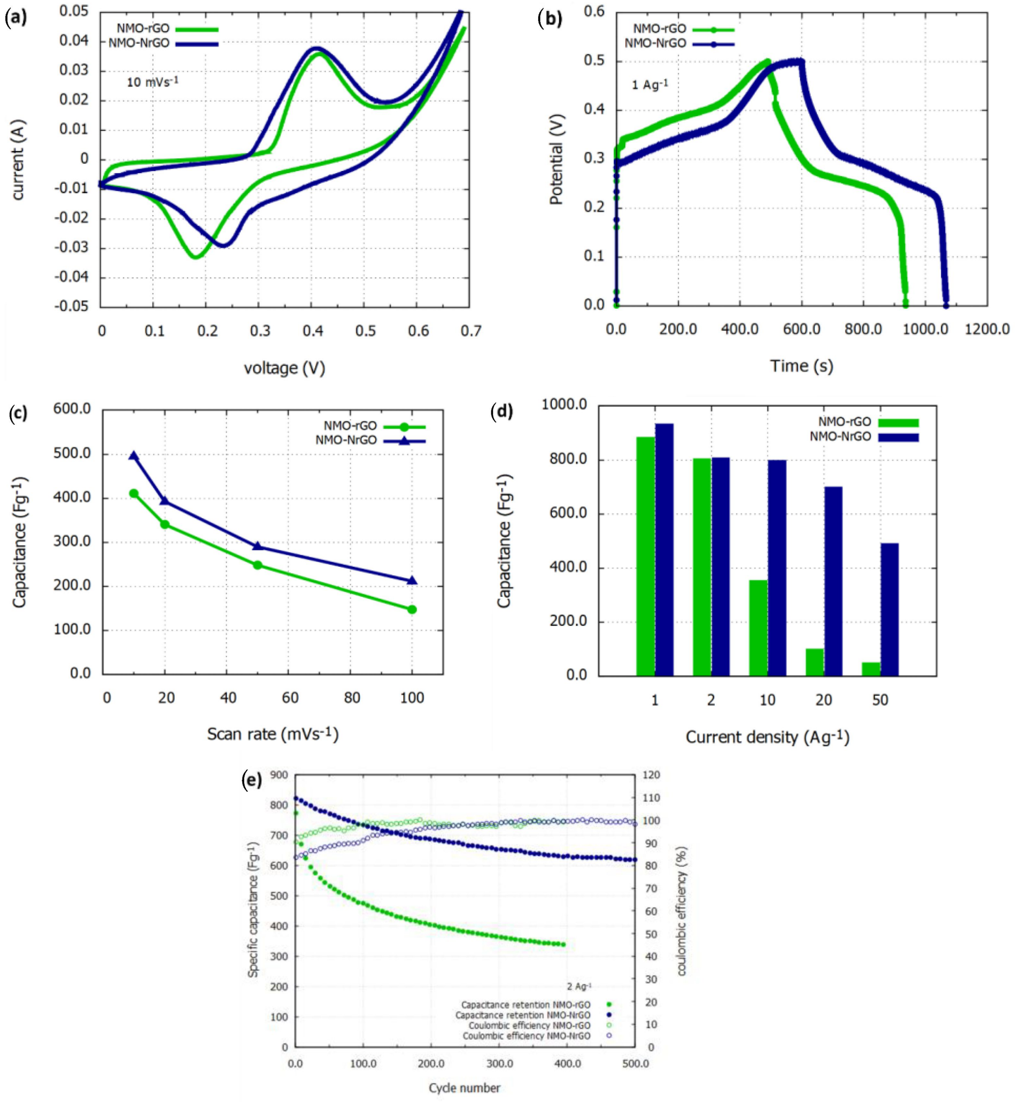

Figure 4. (**a**) Cyclic voltammetry (CV) diagram at a scan rate of 10 mV s^{-1}; (**b**) galvanostatic charge–discharge (GCD) diagram at a current density of 1 Ag^{-1}; (**c**) specific capacitance vs. scan rate; (**d**) specific capacitance vs. current density, and (**e**) cycling performance of NMO-rGO and NMO-NrGO electrodes.

3.3. Electrochemical Properties of an NMO-NrGO//AC Asymmetric Supercapacitor

An asymmetric supercapacitor was fabricated using an NMO-NrGO electrode and AC in 3.0 M KOH. Figure 5a shows the CV diagram of both electrodes, i.e., NMO-NrGO as the cathode and AC as the anode, at a scan rate of 10 mV s^{-1}. In the CV curve of the NMO-NrGO electrode, a pair of oxidation–reduction peaks can be observed, indicating Faradaic reactions and the battery-like behavior of $NiMoO_4$. In contrast, the CV curve of the AC electrode is almost rectangular without oxidation–reduction peaks, which is specific to carbon materials and indicates that the electrical double layer is formed. Based on the specific capacitances of the NMO-NrGO electrode (495.7 Fg^{-1}) and the AC electrode (138.1 Fg^{-1}) at 10 mV s^{-1}, and on the potential range of both electrodes, the mass ratio was calculated as 0.4 m^+/m^- [53,54]. According to this ratio, the amounts of active material on both positive and negative electrodes were considered to be 2 and 5 mg, respectively. Therefore, the voltage window of the NMO-NrGO//AC asymmetric cell can be increased from 0.7 V in a symmetric supercapacitor to 1.1 V in an asymmetric supercapacitor. Figure 5b shows the CV curves of the NMO-NrGO//AC asymmetric supercapacitor in the voltage range of 0–1.1 V and at scan rates of 5–50 mV s^{-1}. All the CV loops display almost rectangular shape and weak redox peaks. The redox peaks in the

CV curves for the NMO-NrGO//AC asymmetric supercapacitor confirm that the charge is stored in the form of Faradaic reactions. In addition, the quasi-rectangular shapes of the CV curves are related to the charge stored in the form of an electrical double-layer capacitive (EDLC) [55]. As can be seen in Figure 5b, up to the voltage of 0.6 V, the supercapacitor stores electrical energy via an electric double layer formed through the physical mechanism, whereas when increasing the working voltage to 0.8 V, it stores the energy in Faradaic form through redox reactions. Furthermore, the CV curves do not display significant changes at high scan rates, indicating the good capacitance of the supercapacitor and its quick response to the current [56]. The maximum specific capacitance for the NMO-NrGO//AC supercapacitor was equivalent to 72.3 Fg^{-1} at a scan rate of 5 mV s^{-1}.

Figure 5c shows the GCD curves of the NMO-NrGO//AC asymmetric supercapacitor in the voltage range of 0–1.1 V and different current densities of 1–20 Ag^{-1}. The nonlinear behavior of the GCD curves caused by redox reactions and the battery-like properties of the metal oxide of $NiMoO_4$ confirm the cathodic and anodic peaks in the CV curves (Figure 5b). The highest calculated specific capacitance (based on the total mass of the active material of two electrodes) was at about 101.2 Fg^{-1} (111.32 Cg^{-1}) at a current density of 1 Ag^{-1}. This supercapacitor maintained its electrochemical efficiency to some extent even at a high current density. Specific capacitance values versus different current densities are given in Figure 5d, illustrating that the specific capacitance decreased with increasing current density. Figure 5d shows a good specific capacitance equivalent to 62 Fg^{-1} at a current density of 20 Ag^{-1}, indicating good electron transfer and ion intercalation abilities. It can be stated that the NMO-NrGO//G supercapacitor has a good ability to store energy at high current densities. Figure 5e shows the cycling performance of the NMO-NrGO//AC asymmetric supercapacitor determined by continuous charge–discharge testing at a current density of 2 Ag^{-1} and in a voltage window of 0–1.1 V. As can be seen, the trend of the specific capacitance during 1000 cycles indicates slight degradation of about 18% during cycling. This implies that the NMO-NrGO//G asymmetric supercapacitor has good stability, likely due to the combination of short intercalation paths in the porous nanostructure of $NiMoO_4$ and the high electrical conductivity of the graphite material. Figure 5f presents an EIS analysis of the NMO-NrGO//AC supercapacitor before and after 1000 cycles over a frequency range of 0.1 Hz–100 KHz. Based on the Nyquist plot, the NMO-NrGO//AC supercapacitor had an internal resistance of ESR = 3.1 Ω and a charge transfer resistance of R_{ct} = 1.43 Ω before the cycling. The internal resistance after the cycling was ESR = 3.4 Ω, which is similar to that before the cycling, indicating good supercapacitor stability. The low internal resistance is due to the large specific surface area and high conductivity of the electroactive material. The charge transfer resistance (R_{ct}) after cycling increased slightly to 2.1 Ω from the initial level. The increase in R_{ct} was probably due to the electroactive material peeling off from the electrode substrate, as a result of decreased adhesion between substrate and active material during the electrochemical performance. In addition, the slope of the linear part of the NMO-NrGO//AC impedance curve before the cycling performance is almost vertical. This indicates lower Warberg resistance (Z_W) and better capacitive behavior before the cycling testing [57]. Z_W is related to the diffusion rate of the OH^- ions intercalating to the electrode. In the Ragone plot, shown in Figure 5g, the energy density and power density [58] of the NMO-NrGO//AC asymmetric supercapacitor synthesized in this work are compared with those of other symmetric and asymmetric supercapacitors reported in the literature. The energy density and power density of the NMO-NrGO//AC supercapacitor investigated here are 17 Wh kg^{-1} and 174.24 kW kg^{-1}, respectively. These are good levels, compared with those of other reported supercapacitors, for example: $NiCo_2S_4$@$NiMoO_4$/NF//AC (21.4 Wh kg^{-1} and 58 kW kg^{-1}) [59], NF@$NiMoO_4$@C//AC (61 Wh kg^{-1} and 21.7 kW kg^{-1}) [60], β-$NiMoO_4$//AC (4.53 Wh kg^{-1} and 252.2 kW kg^{-1}) [61], $NiMoO_4$//AC (54 Wh kg^{-1} and 24 kW kg^{-1}) [45], $MnCo_2O_4$@$NiMoO_4$//AC (42 Wh kg^{-1} and 852.3 kW kg^{-1}) [62], and g-C_3N_4/$NiMoO_4$//rGO (90 Wh kg^{-1} and 300 kW kg^{-1}) [63].

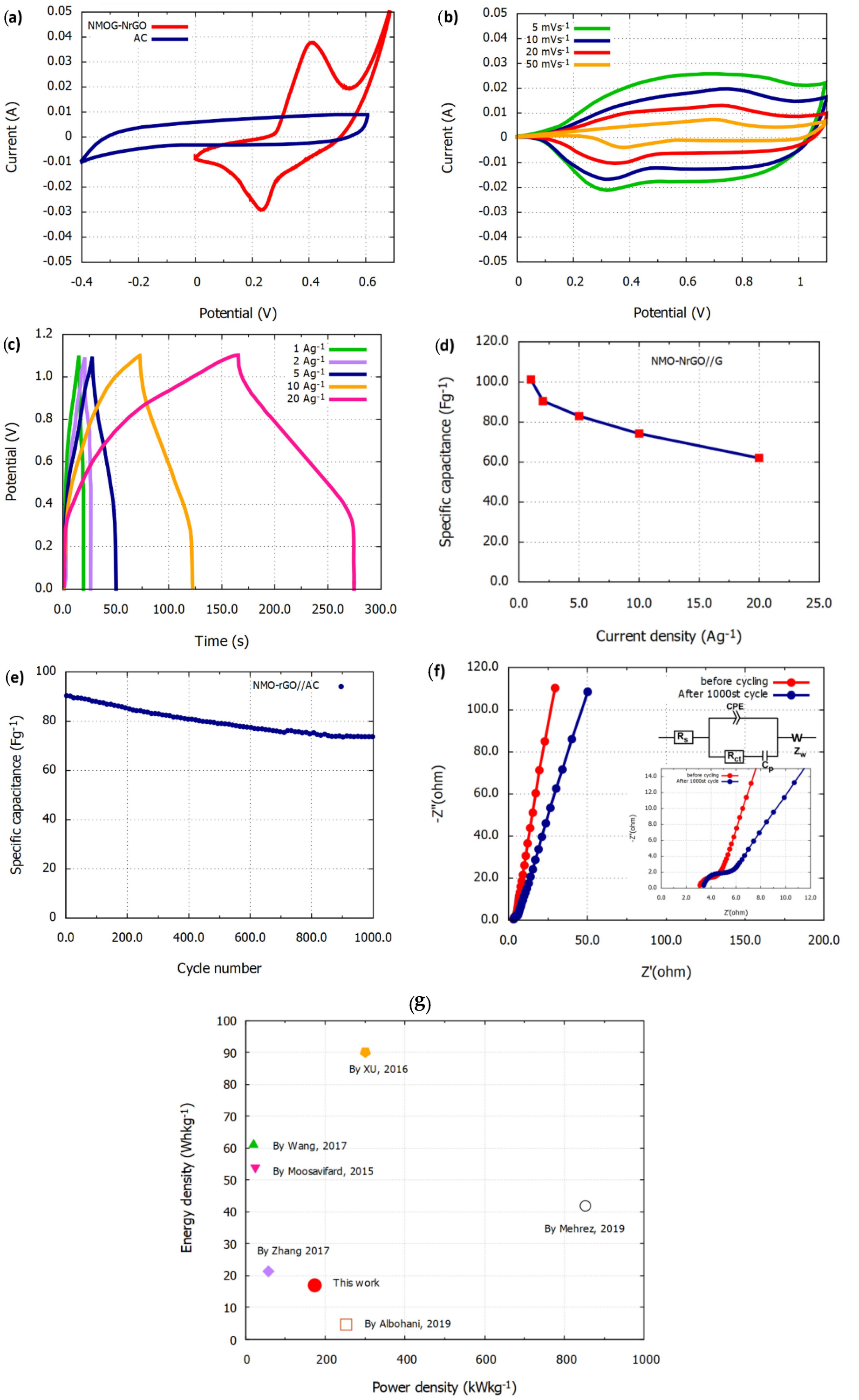

Figure 5. (**a**) CV curves of the NMO-NrGO and AC electrodes at a scan rate of 10 mV s^{-1} in the three-electrode setup; (**b**) CV curves in the voltage range of 0–1.1 V and at various scan rates of 5–50 mV s^{-1}; (**c**) GCD curves with nonlinear behavior at the potential range of 0–1.1 V and at various current densities of 1–20 Ag^{-1}; (**d**) specific capacitance vs. various current densities of 1–20 Ag^{-1}; (**e**) cycling performance at 2 Ag^{-1} after 1000 cycles; (**f**) comparison of the Nyquist plot, before and after 1000 cycles; and (**g**) Ragone plot of the NMO-NrGO//AC asymmetric supercapacitor synthesized here compared with other symmetric and asymmetric supercapacitors reported in the literature (Xu 2016 [60], Wang 2017 [57], Moosavifard 2015 [45], Zhang 2017 [56], Albohani 2019 [58] and Mehraz 2019 [59]).

4. Conclusions

NMO-rGO and NMO-NrGO nanocomposites were prepared using a simple precipitation method in starch medium. The electrochemical performance indicates that NMO-NrGO had a higher specific capacitance of 932 Fg^{-1} (466 Cg^{-1}). This higher specific capacitance is attributed to the greater reduction in negative functional groups on GO sheets, which enhanced the electrical conductivity and eventually the specific capacitance. The maximum specific capacitance of the NMO-NrGO//AC supercapacitor was about 101.2 Fg^{-1} (111.32 Cg^{-1}) at a current density of 1 Ag^{-1}. The cycling performance of the supercapacitor indicated good stability over 1000 cycles with only a slight degradation of 18%. The calculated energy density and power density of the NMO-NrGO//AC supercapacitor were about 17 Wh kg^{-1} and 174.24 kW kg^{-1}, respectively.

Supplementary Materials: The following supporting information can be downloaded at: https://www.mdpi.com/article/10.3390/jcs7060217/s1. Table S1: The primary chemicals used in this work; Figure S1: The Energy dispersive X-ray (EDX) mapping analysis of NiMoO4; Figure S2: CV curves of the NMO-NrGO electrode: (**a**) in 3.0 M H_2SO_4, 3.0 M KOH, and 3.0 M Na_2SO_4 electrolytes; (**b**) in KOH electrolyte with concentrations of 1.0, 2.0, 3.0, and 4.0 M.

Author Contributions: S.A.-R.: investigation, methodology, synthesis, and writing the original-draft, R.S.-M.: supervision; G.R.: formal analysis and editing the manuscript; N.B.: providing laboratory facilities and technical assistance; J.Ö.: editing and formal analysis and H.O.: supervision and editing the article. All authors have read and agreed to the published version of the manuscript.

Funding: This research received no external funding.

Acknowledgments: The authors acknowledge and thank Tarbiat Modares University and Mid Sweden University for supporting this research with laboratory facilities, supervision, and technical assistance.

Conflicts of Interest: The authors declare no conflict of interest.

References

1. Liu, C.; Li, F.; Ma, L.-P.; Cheng, H.-M. Advanced Materials for Energy Storage. *Adv. Mater.* **2010**, *22*, E28–E62. [CrossRef] [PubMed]
2. Li, Y.; Wu, Y.; Li, T.; Lu, M.; Chen, Y.; Cui, Y.; Gao, J.; Qian, G. Tuning the electronic structure of a metal–organic framework for an efficient oxygen evolution reaction by introducing minor atomically dispersed ruthenium. *Carbon Energy* **2023**, *5*, e265. [CrossRef]
3. Shown, I.; Ganguly, A.; Chen, L.-C.; Chen, K.H. Conducting polymer-based flexible supercapacitor. *Energy Sci. Eng.* **2015**, *3*, 2–26. [CrossRef]
4. Karthikeyan, S.; Mahalingam, P. Syntheses and applications of carbon nanotubes and their composites. *Carbon App.* **2013**, *22*, 495–537.
5. Wang, K.; Chen, C.; Li, Y.; Hong, Y.; Wu, H.; Zhang, C.; Zhang, Q. Insight into Electrochemical Performance of Nitrogen-Doped Carbon/NiCo-Alloy Active Nanocomposites. *Small* **2023**, 2300054. [CrossRef]
6. Yue, T.; Shen, B.; Gao, P. Carbon material/MnO_2 as conductive skeleton for supercapacitor electrode material: A review. *Renew. Sustain. Energy Rev.* **2022**, *158*, 112131. [CrossRef]
7. Veeresh, S.; Ganesha, H.; Nagaraju, Y.S.; Vijeth, H.; Vandana, M.; Basappa, M.; Devendrappa, H. Graphene ox-ide/cobalt oxide nanocomposite for high-performance electrode for supercapacitor application. *J. Energy Storage* **2022**, *52*, 104715. [CrossRef]
8. Vinodh, R.; Babu, R.S.; Atchudan, R.; Kim, H.-J.; Yi, M.; Samyn, L.M.; de Barros, A.L.F. Fabrication of High-Performance Asymmetric Supercapacitor Consists of Nickel Oxide and Activated Carbon (NiO//AC). *Catalysts* **2022**, *12*, 375. [CrossRef]
9. Karimi, F.; Korkmaz, S.; Karaman, C.; Karaman, O.; Kariper, A. Engineering of GO/MWCNT/RuO_2 ternary aerogel for high-performance supercapacitor. *Fuel* **2022**, *329*, 125398. [CrossRef]
10. Jinlong, L.; Meng, Y.; Suzuki, K.; Miura, H. Synthesis of $CoMoO_4$@RGO nanocomposites as high-performance supercapacitor electrodes. *Microporous Mesoporous Mater.* **2017**, *242*, 264–270. [CrossRef]
11. Prabhu, S.; Maruthapandi, M.; Durairaj, A.; Arun Kumar, S.; Luong, J.H.; Ramesh, R.; Gedanken, A. Performances of Co^{2+}-substituted $NiMoO_4$ nanorods in a solid-state hybrid supercapacitor. *ACS Appl. Energy Mater.* **2023**, *6*, 1321–1331. [CrossRef]
12. Jayasubramaniyan, S.; Balasundari, S.; Rayjada, P.A.; Satyanarayana, N.; Muralidharan, P. Microwave hydrothermal synthesis of α-$MnMoO_4$ nanorods for high electrochemical performance supercapacitors. *RSC Adv.* **2018**, *8*, 22559–22568. [CrossRef]
13. Liu, X.; Zhang, K.; Yang, B.; Song, W.; Liu, Q.; Jia, F.; Qin, S.; Chen, W.; Zhang, Z.; Li, J. Three-dimensional graphene skeletons supported nickel molybdate nanowire composite as novel ultralight electrode for supercapacitors. *Mater. Lett.* **2016**, *164*, 401–404. [CrossRef]
14. Wu, F.; Liao, Q.; Cao, F.; Li, L.; Zhang, Y. Non-noble bimetallic $NiMoO_4$ nanosheets integrated Si photoanodes for highly efficient and stable solar water splitting. *Nano Energy* **2017**, *34*, 8–14. [CrossRef]

15. Zhang, P.; Zhou, J.; Chen, W.; Zhao, Y.; Mu, X.; Zhang, Z.; Pan, X.; Xie, E. Constructing highly-efficient electron transport channels in the 3D electrode materials for high-rate supercapacitors: The case of $NiCo_2O_4$@$NiMoO_4$ hierarchical nanostructures. *Chem. Eng. J.* **2017**, *307*, 687–695. [CrossRef]
16. Liu, T.; Chai, H.; Jia, D.; Su, Y.; Wang, T.; Zhou, W. Rapid microwave-assisted synthesis of mesoporous $NiMoO_4$ nanorod/reduced graphene oxide composites for high-performance supercapacitors. *Electrochim. Acta* **2015**, *180*, 998–1006. [CrossRef]
17. Kianpour, G.; Salavati-Niasari, M.; Emadi, H. Sonochemical synthesis and characterization of $NiMoO_4$ nanorods. *Ultrason. Sonochem.* **2013**, *20*, 418–424. [CrossRef]
18. Umapathy, V.; Neeraja, P.; Manikandan, A.; Ramu, P. Synthesis of $NiMoO_4$ nanoparticles by sol–gel method and their structural, morphological, optical, magnetic and photocatlytic properties. *Trans. Nonferr. Met. Soc. China* **2017**, *27*, 1785–1793. [CrossRef]
19. Sharma, G.P.; Pala, R.G.S.; Sivakumar, S. Ultrasmall $NiMoO_4$ robust nanoclusters-active carbon composite for high performance extrinsic pseudocapacitor. *Electrochim. Acta* **2019**, *318*, 607–616. [CrossRef]
20. Hao, Y.; Huang, H.; Wang, Q.; Wang, Q.; Zhou, G. Nitrogen-doped carbon/$NiMoO_4$ nanospheres assembled by nanosheets and ultrasmall nanoparticles for supercapacitors. *Chem. Phys. Lett.* **2019**, *728*, 215–223. [CrossRef]
21. Xu, X.; Liu, Q.; Zhang, X. A Novel Hierarchical Flower-like $NiMoO_4$ for Supercapacitors. *Chem. Lett.* **2018**, *47*, 1213–1215. [CrossRef]
22. Chen, J.; Zhao, G.; Chen, Y.; Rui, K.; Mao, H.; Dou, S.X.; Sun, W. Iron-Doped Nickel Molybdate with Enhanced Oxygen Evolution Kinetics. *Chem. A Eur. J.* **2019**, *25*, 280–284. [CrossRef] [PubMed]
23. Wang, K.; Guo, Y.; Zhang, Q. Metal–Organic Frameworks Constructed from Iron-Series Elements for Supercapacitors. *Small Struct.* **2022**, *3*, 2100115. [CrossRef]
24. Qian, H.; Jinlong, L.; Tongxiang, L.; Chen, W. In Situ Synthesis of Mesoporous $NiMoO_4$ on Ball Milled Graphene for High Performance Supercapacitors. *J. Electrochem. Soc.* **2017**, *164*, E173–E179. [CrossRef]
25. Prakash, N.G.; Dhananjaya, M.; Narayana, A.L.; Hussain, O.M. High performance one dimensional α-MoO_3 nanorods for supercapacitor applications. *Ceram. Int.* **2018**, *44*, 9967–9975. [CrossRef]
26. Roy, A.; Ray, A.; Saha, S.; Ghosh, M.; Das, S. NiO-CNT composite for high performance supercapacitor electrode and oxygen evolution reaction. *Electrochim. Acta* **2018**, *283*, 327–337. [CrossRef]
27. Park, G.D.; Hong, J.H.; Lee, J.-K.; Kang, Y.C. Yolk–shell-structured microspheres composed of N-doped-carbon-coated $NiMoO_4$ hollow nanospheres as superior performance anode materials for lithium-ion batteries. *Nanoscale* **2019**, *11*, 631–638. [CrossRef]
28. Yang, S.; Zhang, K. Converting Corncob to Activated Porous Carbon for Supercapacitor Application. *Nanomaterials* **2018**, *8*, 181. [CrossRef]
29. Krishnan, S.G.; Ab Rahim, M.H.; Jose, R. Synthesis and characterization of $MnCo_2O_4$ cuboidal microcrystals as a high performance psuedocapacitor electrode. *Alloy. Compd.* **2016**, *656*, 707–713. [CrossRef]
30. Ossonon, B.D.; Bélanger, D. Synthesis and characterization of sulfophenyl-functionalized reduced graphene oxide sheets. *RSC Adv.* **2017**, *7*, 27224–27234. [CrossRef]
31. Srivastava, M.; Uddin, E.; Singh, J.; Kim, N.H.; Lee, J.H. Preparation and characterization of self-assembled layer by layer $NiCo_2O_4$–reduced graphene oxide nanocomposite with improved electrocatalytic properties. *J. Alloys Compd.* **2014**, *590*, 266–276. [CrossRef]
32. Fayer, M.D. *Ultrafast Infrared Vibrational Spectroscopy*; CRC Press: Boca Raton, FL, USA, 2013.
33. Faniyi, I.O.; Fasakin, O.; Olofinjana, B.; Adekunle, A.S.; Oluwasusi, T.V.; Eleruja, M.A.; Ajayi, E.O.B. The comparative analyses of reduced graphene oxide (RGO) prepared via green, mild and chemical approaches. *SN Appl. Sci.* **2019**, *1*, 1181. [CrossRef]
34. Li, Y.; Jian, J.; Fan, Y.; Wang, H.; Yu, L.; Cheng, G.; Sun, M. Facile one-pot synthesis of a $NiMoO_4$/reduced graphene oxide composite as a pseudocapacitor with superior performance. *RSC Adv.* **2016**, *6*, 69627–69633. [CrossRef]
35. de Moura, A.P.; de Oliveira, L.H.; Rosa, I.L.; Xavier, C.S.; Lisboa-Filho, P.N.; Li, M.S.; Varela, J.A. Structural, optical, and magnetic properties of $NiMoO_4$ nanorods prepared by microwave sintering. *Sci. World J.* **2015**. [CrossRef]
36. Arshadi Rastabi, S.; Sarraf Mamoory, R.; Blomquist, N.; Phadatare, M.; Olin, H. Synthesis of a $NiMoO_4$/3D-rGO nanocomposite via starch medium precipitation method for supercapacitor performance. *Batteries* **2020**, *6*, 5. [CrossRef]
37. Yousefi, R.; Mahmoudian, M.; Sa'aedi, A.; Cheraghizade, M.; Jamali-Sheini, F.; Azarang, M. Effect of annealing temperature and graphene concentrations on photovoltaic and NIR-detector applications of PbS/rGO nanocomposites. *Ceram. Int.* **2016**, *42*, 15209–15216. [CrossRef]
38. Arshadi Rastabi, S.; Sarraf Mamoory, R.; Dabir, F.; Blomquist, N.; Phadatare, M.; Olin, H. Synthesis of Ni-MoO_4/3D-rGO nanocomposite in alkaline environments for supercapacitor electrodes. *Crystals* **2019**, *9*, 31. [CrossRef]
39. Bankar, P.K.; Ratha, S.; More, M.A.; Late, D.J.; Rout, C.S. Enhanced field emission performance of $NiMoO_4$ nanosheets by tuning the phase. *Appl. Surf. Sci.* **2017**, *418*, 270–274. [CrossRef]
40. Ehsan, M.A.; Khan, A. Aerosol-Assisted Chemical Vapor Deposition Growth of $NiMoO_4$ Nanoflowers on Nickel Foam as Effective Electrocatalysts toward Water Oxidation. *ACS Omega* **2021**, *6*, 31339–31347. [CrossRef]
41. Li, G.L.; Qiao, X.Y.; Miao, Y.Y.; Wang, T.Y.; Deng, F. Synergistic Effect of N-$NiMoO_4$/Ni Heterogeneous Interface with Oxygen Vacancies in N-$NiMoO_4$/Ni/CNTs for Superior Overall Water Splitting. *Small* **2023**, 2207196. [CrossRef]
42. Azarang, M.; Shuhaimi, A.; Yousefi, R.; Sookhakian, M. Effects of graphene oxide concentration on optical properties of ZnO/RGO nanocomposites and their application to photocurrent generation. *J. Appl. Phys.* **2014**, *116*, 084307. [CrossRef]

43. Oudghiri-Hassani, H.; Al Wadaani, F. Preparation, Characterization and Catalytic Activity of Nickel Molybdate ($NiMoO_4$) Nanoparticles. *Molecules* **2018**, *23*, 273. [CrossRef] [PubMed]
44. Yang, J.; Liu, W.; Niu, H.; Cheng, K.; Ye, K.; Zhu, K.; Yan, J. Ultrahigh energy density battery-type asymmetric su-percapacitors: NiMoO4 nanorod-decorated graphene and graphene/Fe_2O_3 quantum dots. *Nano Res.* **2018**, *11*, 4744–4758. [CrossRef]
45. Moosavifard, S.E.; Shamsi, J.; Ayazpour, M. 2D high-ordered nanoporous $NiMoO_4$ for high-performance super-capacitors. *Ceram. Int.* **2015**, *41*, 1831–1837. [CrossRef]
46. Arshadi Rastabi, S.; Sarraf-Mamoory, R.; Razaz, G.; Blomquist, N.; Hummelgård, M.; Olin, H. Treatment of Ni-MoO_4/nanographite nanocomposite electrodes using flexible graphite substrate for aqueous hybrid supercapacitors. *PLoS ONE* **2021**, *16*, e0254023. [CrossRef]
47. Guo, D.; Zhang, P.; Zhang, H.; Yu, X.; Zhu, J.; Li, Q.; Wang, T. $NiMoO_4$ nanowires supported on Ni foam as novel advanced electrodes for supercapacitors. *J. Mater. Chem. A* **2013**, *1*, 9024–9027. [CrossRef]
48. Vlad, A.; Singh, N.; Rolland, J.; Melinte, S.; Ajayan, P.M.; Gohy, J.-F. Hybrid supercapacitor-battery materials for fast electrochemical charge storage. *Sci. Rep.* **2014**, *4*, 4315. [CrossRef]
49. Nakanishi, H.; Kikuta, I.; Kawabata, Y.; Norisuye, T.; Tran-Cong-Miyata, Q.; Segawa, H. Fast Ion and Electron Transport in a Supercapacitor Based on Monolithic Nanowire-Array Electrodes Prepared from a Defect-Free Anodic Alu-minium Oxide Mold. *Adv. Mater. Interfaces* **2015**, *2*, 1500354. [CrossRef]
50. Guo, D.; Luo, Y.; Yu, X.; Li, Q.; Wang, T. High performance NiMoO4 nanowires supported on carbon cloth as advanced electrodes for symmetric supercapacitors. *Nano Energy* **2014**, *8*, 174–182. [CrossRef]
51. Zhong, C.; Deng, Y.; Hu, W.; Qiao, J.; Zhang, L.; Zhang, J. A review of electrolyte materials and compositions for electrochemical supercapacitors. *Chem. Soc. Rev.* **2015**, *44*, 7484–7539. [CrossRef]
52. Gilliam, R.; Graydon, J. A review of specific conductivities of potassium hydroxide solutions for various concentrations and temperatures. *Int. J. Hydrogen Energy* **2007**, *32*, 359–364. [CrossRef]
53. Budhiraju, V.S.; Kumar, R.; Sharma, A.; Sivakumar, S. Structurally stable hollow mesoporous graphitized carbon nanofibers embedded with $NiMoO_4$ nanoparticles for high performance asymmetric supercapacitors. *Electrochim. Acta* **2017**, *238*, 337–348. [CrossRef]
54. Zhang, L.; Zheng, D.; Pei, S.; Ye, L.; Geng, S.; Lian, J. Rational fabrication of nanosheet-dewy $NiMoO_4$/Ni_3S_2 nanohybrid for efficient hybrid supercapacitor. *J. Alloys Compd.* **2019**, *783*, 399–408. [CrossRef]
55. Wang, K.; Wang, Z.; Liu, J.; Li, C.; Mao, F.-F.; Wu, H.; Zhang, Q. Enhancing the Performance of a Battery–Supercapacitor Hybrid Energy Device Through Narrowing the Capacitance Difference Between Two Electrodes via the Utilization of 2D MOF-Nanosheet-Derived Ni@Nitrogen-Doped-Carbon Core–Shell Rings as Both Negative and Positive Electrodes. *ACS Appl. Mater. Interfaces* **2020**, *12*, 47482–47489. [CrossRef]
56. Ramya, A.V.; Thomas, R.; Balachandran, M. Mesoporous onion-like carbon nanostructures from natural oil for high-performance supercapacitor and electrochemical sensing applications: Insights into the post-synthesis sonochemical treatment on the electrochemical performance. *Ultrason. Sonochem.* **2021**, *79*, 105767. [CrossRef]
57. Yue, X.; Chen, Z.; Xiao, C.; Song, G.; Zhang, S.; He, H. Synthesis of CNT@ CoS/NiCo Layered Double Hydroxides with Hollow Nanocages to Enhance Supercapacitors Performance. *Nanomaterials* **2022**, *12*, 3509. [CrossRef]
58. Yazar; Sibel; Arvas, M.B.; Sahin, Y. An ultrahigh-energy density and wide potential window aqueous electrolyte supercapacitor built by polypyrrole/aniline 2-sulfonic acid modified carbon felt electrode. *Int. J. Energy Res.* **2022**, *46*, 8042–8060. [CrossRef]
59. Zhang, Y.; Xu, J.; Zheng, Y.; Zhang, Y.; Hu, X.; Xu, T. $NiCo_2S_4$@$NiMoO_4$ Core-Shell Heterostructure Nanotube Arrays Grown on Ni Foam as a Binder-Free Electrode Displayed High Electrochemical Performance with High Capacity. *Nanoscale Res. Lett.* **2017**, *12*, 412. [CrossRef]
60. Wang, Z.; Wei, G.; Du, K.; Zhao, X.; Liu, M.; Wang, S.; Zhou, Y.; An, C.; Zhang, J. Ni Foam-Supported Carbon-Sheathed $NiMoO_4$ Nanowires as Integrated Electrode for High-Performance Hybrid Supercapacitors. *ACS Sustain. Chem. Eng.* **2017**, *5*, 5964–5971. [CrossRef]
61. Albohani, S.; Sundaram, M.M. Egg shell membrane template stabilises formation of β-$NiMoO_4$ nanowires and en-hances hybrid supercapacitor behaviour. *Mater. Lett.* **2019**, *236*, 64–68. [CrossRef]
62. Mehrez JA, A.; Owusu, K.A.; Chen, Q.; Li, L.; Hamwi, K.; Luo, W.; Mai, L. Hierarchical $MnCo_2O_4$@$NiMoO_4$ as Free-Standing Core-Shell Nanowire Arrays with Synergistic Effect for Enhanced Supercapacitor Performance. *Inorg. Chem. Front.* **2019**, *1*, 857–865. [CrossRef]
63. Xu, X.; Liu, Q.; Wei, T.; Zhao, Y.; Zhang, X. Enhanced energy storage activity of $NiMoO_4$ modified by graphitic carbon nitride. *J. Mater. Sci. Mater. Electron.* **2019**, *30*, 5109–5119. [CrossRef]